Intrafibrillar mineralization and immunomodulatory for synergetic enhancement of bone regeneration via calcium phosphate nanocluster scaffold

Yanyan Zhou#, Zihe Hu#, Wenjing Jin, Haiyan Wu, Minghao Zuo, Changyu Shao, Yanhua Lan, Yang Shi, Ruikang Tang, Zhuo Chen, Zhijian Xie, Jue Shi**

Dedication

Yanyan Zhou and Zihe Hu should be considered joint first author.

Jue Shi and Zhijian Xie should be considered joint corresponding author.

Yanyan Zhou, Zihe Hu, Dr. Wenjing Jin, Haiyan Wu, Minghao Zuo, Dr.Changyu Shao, Yanhua Lan, Yang Shi, Prof. Zhuo Chen, Prof. Zhijian Xie, Dr. Jue Shi

Stomatology Hospital, School of Stomatology, Zhejiang University School of Medicine, Clinical Research Center for Oral Diseases of Zhejiang Province, Key Laboratory of Oral Biomedical Research of Zhejiang Province, Cancer Center of Zhejiang University, Hangzhou 310006, China.

Ruikang Tang

Center for Biomaterials and Biopathways, Department of Chemistry, Zhejiang University, Hangzhou, Zhejiang, 310027, China.

E-mail: dentistsj@zju.edu.cn, xzj66@zju.edu.cn

This article has been accepted for publication and undergone full peer review but has not been through the copyediting, typesetting, pagination and proofreading process, which may lead to differences between this version and the Version of Record. Please cite this article as doi: 10.1002/adhm.202201548.

Abstract:

Inspired by the bionic mineralization theory, organic-inorganic composites with hydroxyapatite nanorods orderly arranged along collagen fibrils have attracted extensive attention. Planted with an ideal bone scaffold will contribute greatly to the osteogenic microenvironment; however, it remains challenging to develop a biomimetic scaffold with the ability to promote intrafibrillar mineralization and simultaneous regulation of immune microenvironment *in situ*. To overcome these challenges, a scaffold containing ultra-small particle size calcium phosphate nanocluster (UsCCP) was prepared, which could enhance bone regeneration through the synergetic effect of intrafibrillar mineralization and immunomodulatory. By efficient infiltration into collagen fibrils, the UsCCP released from the scaffold achieved intrafibrillar mineralization. It also promoted the M2 type polarization of macrophages, leading to an immune microenvironment with both osteogenic and angiogenic potential. The results confirmed that the UsCCP scaffold had both intrafibrillar mineralization and immunomodulatory effects, making it a promising candidate for bone regeneration.

1. Introduction

The growing incidence of bone injuries has led to an increasing demand for rapid and effective therapies to heal defective bone. Bone transplantation is now a well-established treatment for bone defects; however, the source of autologous bone grafts is limited and allogeneic bone may develop immune responses.[1,2] These limitations have stimulated the rapid development of bone tissue engineering. With the advancement of bionics, biomaterials mimicking the structural, mechanical and biological characteristics of natural tissues have attracted extensive attention.[3,4] Haversian bone-mimicking scaffolds improve the capacity of cells to reside in the graft based on their structural design, demonstrating great potential in accelerating blood vessel growth and facilitating new bone formation.[5] Bionic collagen nano-hydroxyapatite scaffolds with optimized structure possess high biocompatibility, superior mechanical properties, osteoconductivity, and osteoinductivity.[6]

Triggered by the biological cues of natural bone, bone regeneration requires macroscopic tissue alignment and microscopic structural repair, whereas biomimetic strategies to facilitate bone healing at the nanoscale have been rarely reported.

Biomineralization is a common process in nature, in which organisms form minerals with multi-level ordered structure, including the bones and teeth of vertebrates.[7] Natural bone is a complex tissue with hierarchical structures and remarkable mechanical properties in terms of hardness and toughness.[8] These properties are attributed to the collagen fibers that are densely mineralized with hydroxyapatite nanoparticle and aligned unidirectionally, forming the basic composite of native bone. [9,10] As such, the biomineralization of collagen is necessary for the unique physiological and mechanical properties of these tissues. Notably, amorphous calcium phosphate (ACP) is the precursor phase for bone formation.[11,12] With the development of biomineralization, increasing evidence shows that the small-sized ACP precursor phase can penetrate into collagen fibers, deposit in the internal nanoscale space, and promote intrafibrillar mineralization through the formation of co-oriented arrays of lamellar hydroxyapatite (HAP) crystal within the fibrils.[4,13,14] Small-sized calcium phosphate has been synthesized and used as the mineral source of biomineralization.[15-17] Great progress has been achieved in the exploration of intrafibrillar mineralization and the development of composite materials with natural bone composition and structure.[18] Zhou et al. proposed a calcium phosphate prenucleation clusters (CaP-PNCs)/starch complex, which included amorphous calcium phosphate nanoclusters and could repair tooth tissue defects. The CaP-PNCs/starch complex provided a smart mineral source supply for biomimetic mineralization and a new pathway for the design of biomimetic materials.[19] Xu et al. noted that CMC is a biodegradable, biocompatible, non-toxic and antibacterial material, which could stabilize ACP in solution to form amorphous nanoprecursors. Hence, they prepared a CMC/ACP scaffold and realized the mineralization of dentine collagen fibers. However, the effect of small size was ignored, and the direct roles of cells and materials were overlooked.[20] Yao et al. prepared small-sized calcium

phosphate with polyacrylic acid (PAA) and polyaspartic acid (PASP) as stabilizers. It achieved 95% collagen mineralization *in vitro* and effectively repaired the tibia of osteoporosis mice.[21] Many studies suggested that small-sized calcium phosphate plays an excellent role in promoting intrafibrillar mineralization, and stable preparation methods of small size calcium phosphate have been proposed.[22,23] Nevertheless, the safe and effective stable preparation technology of calcium phosphate at the nanoscale is still challenging for material applications.

The role of ACP in bone biomineralization has been widely recognized, and ACP is increasingly applied in the development of biomaterials as implant materials to repair bone tissue. Wei Teng et al. synthesized mineralized collagen fibers and ACP to mimic the components and hierarchical structure of woven bone to preserve the alveolar ridge.[24] However, immune responses initiated by the implantation of bone biomaterials significantly affected the wound healing and tissue remodeling process.[25,26] A beneficial immune microenvironment modulated by biomaterials could promote bone healing and regeneration.[27] Materials inducing the transition of immune cells from an inflammatory to an anti-inflammatory phenotype exhibit enhanced bone inductivity.[28,29] Thus, ideal bone scaffolds should provide an excellent osteogenic microenvironment. A great number of products (e.g., ions, functional groups and biomolecules) are released from biomaterials into the microenvironment after the implantation of ACP biomaterials, prompting the body's immune response and triggering a cascade response.[30,31] The exact chemical composition[32], crystallinity[33] and particle size[10] of the organic-inorganic composite calcium phosphate material will affect the polarization of macrophages, which can result in different effects during tissue repair. Compared with HAP or bone with high crystallinity, the small-sized ACP phase has higher solubility, can act on macrophages faster, and cause a minor inflammatory response.[34,35] Additionally, studies have extensively suggested that small particles escape more easily after being endocytosed by cells, while large particles stay within the cells and cause damage.[36,37] The above researches revealed that the small particle size of ACP seems to be more conductive for immune regulation. It is challenging to

develop a biomimetic ultra-small particle size composite scaffold that can simultaneously promote intrafibrillar mineralization and regulate the immune microenvironment *in situ*.

In this study, we prepared a scaffold containing ultra-small particle size of about 1.88 ± 0.26 nm calcium phosphate nanocluster (UsCCP) with carboxymethyl chitosan (CMC) and polyaspartic acid (PASP) as stabilizers. The existing research suggests that PASP, a non-collagenous protein, directs the crystal nucleation.[38] CMC has the benefits of being non-toxic, degradable and low immunogenicity.[39] As an amphoteric electrolyte, it has been generally used to stabilize ACP.[40] The UsCCP in the scaffold, as an inorganic filler, could significantly promote intrafibrillar mineralization. Subsequently, the immunomodulatory effects of this UsCCP released from the scaffold on macrophages, the osteogenic effect of the activated bone immune environment on mouse bone marrow stromal cells (mBMSCs), and the angiogenesis effect on human umbilical vein endothelial cells (HUVECs) were investigated. In brief, an organic-inorganic scaffold containing UsCCP was developed, and its regulatory effect on macrophages was evaluated. It could synergistically induce intrafibrillar mineralization, and is expected to achieve an orderly biomimetic regulation of bone healing and guide effective bone tissue regeneration (Figure 1A).

2. Results and Discussion

2.1 Preparation and properties of UsCCP.

In this study, we fabricated a scaffold containing UsCCP. High concentrations of Ca^{2+}/PO_4^{3-} can be stabilized in UsCCP with two biocompatible polymer additives, CMC and PASP. Due to the introduction of carboxymethyl groups into CMC, it could be used as an anionic polymer below its isoelectric point, enabling chelation with more Ca^{2+}.[41] Moreover, its anti-inflammatory properties have been proved by many researches, which led to the application of carboxymethyl chitosan as a potential organic stabilizer in the UsCCP scaffold.[42] However, this polymer also leads to

precipitation when mixed with a high concentration of Ca^{2+}.[43] Thus, we adopted PASP combined with Ca^{2+} as the CMC competitor. A considerable number of negatively charged carboxylic acid groups on the CMC and PASP side chain could bind Ca^{2+} and prevent Ca^{2+} from precipitating with PO_4^{3-} immediately, forming a more stable calcium phosphate nanocluster. Besides, we conducted a series of tests to verify that the prepared scaffold contains UsCCP. The mineral phase formed was observed with high-resolution transmission electron microscopy (HRTEM), and its orientation was analyzed by the Selected Area Electron Diffraction (SAED) (Figure 1B). The cluster size was around 1.88 ± 0.26 nm and the clusters seemed to consist of amorphous material (inset of Figure 1B). The prepared solution containing UsCCP could be lyophilized to obtain the scaffold (Figure 1C). The Fourier Transform Infrared Spectroscopy (FTIR) results in Figure 1D exhibit the phases in the UsCCP scaffold. The broad absorption bands at about 1062 cm^{-1} (phosphate stretching (v3)) and 542 cm^{-1} (phosphate bending (v4)) and broad X-ray diffraction (XRD) (Figure 1E) diffraction patterns suggested the amorphous nature of the material. These experimental results all verified that the substance contained in UsCCP scaffold was ultra-small calcium phosphate nanocluster. The internal morphology of UsCCP scaffold was observed by scanning electron microscope (SEM) (Figure 1F1, F2). The results revealed that the UsCCP scaffold has a uniform porous structure, with nanopores nested in micrometer-sized pores, and the porosity of UsCCP scaffold was 51.08%. In this way, it can mimic the natural extracellular matrix, support cell adhesion and proliferation, and provide sufficient space and nutrition.[44,45] The energy spectrum of Energy Dispersive Spectroscopy (EDS) showed that the calcium and phosphorus elements were evenly distributed in scaffold (Figure 1G1, 2). The degradation of UsCCP scaffold was performed (Figure S1), with a weight loss of approximately 89 wt% after 10 days. Mechanical property of UsCCP scaffold was studied with compression test. The result showed that compression modulus of scaffold was taken as the slope value at 3% strain (figure S2) and the value was 2.04 ± 0.162 Mpa. Overall, a stable preparation technique was provided for the synthesis of a scaffold containing UsCCP.

2.2 Collagen intrafibrillar mineralization

Intrafibrillar minerals are critical for the desirable mechanical properties of collagen fibril and the biomimetic regeneration of hard tissues. The strength and toughness of bone are based on the degree of mineralization within the fibers.[46-48] Therefore, HRTEM was used to test the mineralization effect of UsCCP on collagen fibers, and the results were illustrated in Figure 2A-D. When co-cultured with the UsCCP scaffold, since the scaffolds could be gradually dissolved in solution to release UsCCP, UsCCP could be observed on the surface of collagen fibrils at 1 h (Figure S3). The collagen fibrils were partially mineralized within 12 h (Figure 2C), and most of them were mineralized within 24 h (Figure 2D). At the same time, we added the HAP group as a comparison to conduct the collagen intrafibrillar mineralization experiment. Most mineral deposits formed in the finished HAP group were located outside the collagen fibers (Figure 2B). To compare the effects of large size ACP (LsACP) and UsCCP in promoting intrafibrillar mineralization, the LsACP group was added. HRTEM results showed that the LsACP were spherical particles with a diameter of 72.43 ± 13.86 nm (Figure S4 A) and the results indicated that no intra-collagen mineralization occurred at 12h and 24h (Figure S4 B, C). Under a high-resolution transmission electron microscope, the collagen fibrils of the UsCCP group (Figure 2E) demonstrated that the mineral crystals in the fibers grew toward the long axis of the collagen fibrils. The SAED presented a typical arc pattern, confirming that the mineral phase was HAP. The lattice fringe of the mineral in the mineralized collagen fibril was observed by HRTEM, the interplanar distance was calculated, which one of was 0.339 nm, matching with (002) plane of HAP (Figure S5). In addition, (002) diffraction arches of the mineralized collagen SAED patterns appeared with symmetrical arches, suggesting that the HAP crystal arrangement was aligned along the c-axis of collagen fibers, which was consistent with the characteristics of mineralized collagen in biological bones.[38] The element map inspection showed that the calcium and phosphate elements in the fiber were evenly distributed (Figure 2F1-4). Stochastic Optical Reconstruction Microscopy (STORM) technology can achieve sub-diffraction accuracy to confirm the

intra-fibrous mineralization of type I collagen fibers.[49] Figures 2G1-4 clearly illustrate the spatial relationship of minerals in collagen fibrils. In the three-dimensional (3D) image, fluorescent molecules are distributed along the z-axis, where red and green represent the fluorescence of collagen and calcium phosphate, respectively, and yellow is formed by the spatial superposition of red collagen and green calcium phosphate, indicating that mineral deposits were located inside collagen fibers. Therefore, benefiting from the intrafibrillar mineralization realized by UsCCP, a relatively uniform structure with the integration of calcium phosphate mineral phase within the fibril was achieved. STORM sub-diffraction accuracy and 3D-Storm provided mineralization along different z-axes, thus confirming intrafibrillar mineralization.

2.3 Regulation of the inflammatory microenvironment and immune response of macrophages.

There are different regulatory mechanisms at different stages of bone healing, including early inflammation, immune regulation, angiogenesis, osteogenic differentiation, and biomineralization, which involve the interactions of multiple cells.[50] The implantation of biomaterials may cause inflammation and local tissue damage by activating macrophages, and prolong wound healing. Therefore, the interaction between implanted biomaterials and immune response is inevitable and should be emphasized. Macrophages dynamically regulate the formation and repair of natural bone, and produce abundant, multi-type and constantly changing cytokines. During this process, macrophages are firstly transformed into M1-type macrophages and secrete pro-inflammatory factors. During the repair process, M1-type macrophages transform into M2-type, which participate in anti-inflammatory and tissue repair. This suggests that better bone healing effect can be achieved by the timely termination of pro-inflammatory response by optimizing M1-M2 conversion at the early stage of bone injury. When the material comes into contact with tissue, it gradually degrades and releases bioactive substances that alter the surrounding bone marrow microenvironment.[51] The release of Ca^{2+} into the local environment has been confirmed as the key for osteoinduction,

which can stimulate the gradual inflammatory response by forming calcium phosphate in the biomaterial/tissue microenvironment.[52-54] Calcium is an effective anti-inflammatory component in the formulation: as a divalent cation, it can affect the polarization of macrophages.[55] Therefore, the UsCCP scaffold was co-coltured with macrophages, and used inductively coupled plasma mass spectrometry (ICP-MS) to detect the change in calcium and phosphorus ion concentrations in the medium on day 1 and 2. In this experiment, the pure medium was used as the positive control, and CMC/PASP was taken as the negative control. Figure S6 shows that the content of calcium ions in the medium of UsCCP group was significantly higher than that in the other two groups, and the increase was about 30 ppm compared with the Control group. Due to the introduction of exogenous calcium ions in the UsCCP group, the calcium ion content continued to rise, while the Ca^{2+} concentration increase in the UsCCP group was lower than that in the other two groups on the second day compared with the first day. This may have been induced by the formation of calcium phosphate and the elevation of macrophage numbers. Endocytosis takes up part of the calcium ions. Similarly, the content of phosphate ions was the highest in the UsCCP group.

The pH value of human body fluids is stably maintained between 7.35-7.45, which is called acid-base balance. With the release of degradation products of biological materials, the pH value of the environment around the materials change, subsequently affecting the functions of cells related to tissue regeneration.[40] Studies have suggested that the polarization state of macrophages is also pH-dependent. The alkaline environment (pH=8.4) can facilitate the proliferation of macrophages and contribute to the polarization of M1 macrophages. With the decrease in pH, macrophages tend to polarize towards the M2 phenotype.[56] Accordingly, changes in the environmental pH value can indicate the state of macrophages. It is urgent to detect the pH change in the cultured environment of macrophages when they are co-cultured with materials. Our test results (Figure S7) demonstrated that the pH value of the medium generally increased on the first day. This increase in the UsCCP

group was particularly significant and reached about 8.25. The environmental pH decreased rapidly over time and dropped to about 7.5 on the third day.

The scaffold was co-cultured with RAW 267.4 cells through transwell migration assay to clarify the bone immunomodulatory effect of UsCCP scaffold (Figure 3A). The effect of UsCCP scaffold on the vitality, proliferation and adhesion of RAW 267.4 cells was investigated. The results of the live/dead assay are depicted in Figure S8. With the passage of time, all groups had increased live cell numbers, while the UsCCP group had a significantly higher number of living cells than the Control group. On the contrary, the UsCCP group had the fewest dead cells (Figure S8a, b). Image J was used to count the number of live and dead cells in different groups. The results showed that, compared with the Control group and the CMC/PASP group, the number of live cells in the UsCCP group was significantly increased (Figure S8c, d). The CCK-8 results were in consistent with the live-dead assay data (Figure S9). Thus, it was established that UsCCP and CMC/PASP groups facilitated the proliferation of macrophages, and the effect of UsCCP group was particularly significant. Changes in the cell morphology were related to different functional states of cells, including cell proliferation and apoptosis, stem cell differentiation, and macrophage polarization.[57,58] It has been demonstrated that the cell shape of polarized macrophages undergoes significant changes, and M2 macrophages exhibit a slender shape compared with M0/M1 macrophages.[59] The results for cytoskeleton and nucleus staining of RAW264.7 cells cultured with different groups for 1 and 2 days are presented in Figure 3B. On the first day, cells of the UsCCP group appeared to attach and spread more conspicuous in comparison to CMC/PASP group, and cells of the Control group were rounded in shape with multiple pseudopodia protruding. On day 2, the cells cultured in UsCCP group became larger and elongated, and exhibited a spindle shape with significant M2 activation characteristics. While cells on Control and CMC/PASP groups remained a similar oval shape with no filopodial extensions. These results suggested that UsCCP released from the scaffold promoted cell stretching and spreading compared with other groups. In summary, the CCK-8, live/dead and cytoskeleton

staining assays initially revealed that UsCCP had good biocompatibility and could promote cell proliferation.

Other tests were conducted to further explore the regulatory effect of UsCCP on the polarization of RAW264.7 cells. The ratio of M1 and M2 of RAW264.7 cells was checked by flow cytometry (Figure 3C). At the same time, FlowJo V10 was used to quantify the percentage of CD11c and CD163 positive cells. As indicated in Figure 3E, on day 1, the number of CD11c and CD163 positive cells was limited in all groups, while the proportion of M1 and M2 cells in the UsCCP group was higher than that in other groups. On day 2, the expression of CD11c in the UsCCP group was slightly downregulated, while the expression level of CD163 was significantly upregulated compared to the other two groups. Moreover, immunofluorescence staining was performed to evaluate the expression of interleukin-1 receptor 1 (IL-1R1, green, a pro-inflammatory marker) and arginase-1 (Arg-1, red, an anti-inflammatory marker) in RAW264.7 cells after being cultured for 1 and 2 days. Consistent with the results of flow cytometry, the expression trend of Arg-1 on days 1 and 2 was UsCCP > CMC/PASP > Control, and the opposite trend was detected in the expression of IL-1R1 (Figure 3D and S10). Regarding the result for day 1, the M1 and M2 indicators increased at the same time. This was probably because UsCCP released from the scaffold could activate macrophages quickly and respond faster to the surrounding environment, leaving macrophages in a state of differentiation. Because of the exposure to the biological material as an exogenous foreign body, the activated macrophages also speeded up the conversion and utilization of UsCCP scaffold in the body. On day 2, the milder inflammatory response subsided, and the activated macrophages transformed into the M2 type that was conducive to tissue remodeling and repair. Then, reverse transcription-polymerase chain reaction (RT-PCR) and western blot assays were employed to detect the expression of related inflammatory genes and proteins in the cells. The results of RT-PCR (Figure 3G) suggested that on day 1, UsCCP group not only up-regulated the gene expression of inflammatory cytokines (IL-1β, INOS, IL-6, and TNF-α) but also increased the gene expression of anti-inflammatory cytokines (Arg-1,

IL-4, IL-10, IL-1Ra). Meanwhile, the gene expression of M1 and M2 markers (CD86 and CD206) was increased. On day 2, the expression of inflammatory cytokine genes in the UsCCP group began to decline, while the anti-inflammatory cytokine maintained a considerable expansion. Moreover, Arg-1 and INOS protein, which are polarization markers of RAW264.7 cells, were detected by Western blot. Compared with the Control group, the expression of Arg-1 and INOS in the UsCCP group and the CMC/PASP group increased on day 1, and that of the UsCCP group slightly increased compared with the CMC/PASP group (Figure 3F and S11). On day 2, compared with the Control group, the expression of Arg-1 in UsCCP group significantly increased, while the expression of INOS did not change remarkably. These data were consistent with flow cytometry and immunofluorescence staining data, implying that UsCCP caused a milder inflammatory response and promoted macrophage M2 polarization.

In order to compare LsACP and UsCCP scaffold on the immune regulation of macrophages, LsACP was co-cultured with RAW264.7 cells. Immunofluorescence staining results showed that the expression of IL-1R1 in LsACP was much higher than that in UsCCP group, and the expression of Arg-1 in LsACP was much lower than that in UsCCP. Fluorescence quantitative results showed that there was a significant difference between the two groups (Figure S12A, B). The results of RT-PCR (Figure S12C) suggested that LsACP group up-regulated the gene expression of inflammatory cytokines on day1 and 2. These data implied that UsCCP released from the scaffold caused a milder inflammatory response and promoted macrophage M2 polarization, while LsACP showed stronger inflammatory response.

2.4 Response of mBMSCs and HUVECs to the macrophage inflammatory microenvironment.

Bone immunomodulation involves interactions between biological materials, immune and bone cells. The immune system and the skeletal system share many regulatory molecules, including cytokines, chemokines, receptors, and transcription factors.[60] Bone formation and vascularization are mutually

coupled phenomena during bone development and growth, which have been widely investigated.[61] Different biomaterials can have different osteogenic inductive abilities by regulating the polarization and functional state of macrophages.[32] Figure S13 presents the analysis of the expression levels of genes related to osteogenesis and angiogenesis in RAW 264.7 cells, which suggests that the cells have a reparative potential. Therefore, the response of mBMSCs and HUVECs to the inflammatory microenvironment induced by biomaterials and macrophages was tested to further evaluate the osteogenic effects of UsCCP. A conditioned medium was used as an indirect co-culture mode to detect the effects of inflammation-related cytokines on mBMSCs and HUVECs (Figure 4A).[62] The character of mBMSCs was identified using flow cytometry. The results suggested that mBMSCs strongly expressed a high level of the mesenchymal stem cell markers CD29 and CD90 and exhibited the negative expression of the hematopoietic cell markers CD34 and CD45 (Figure S14).

Alkaline phosphatase (ALP) activity has been used as an initial indicator of osteoblast differentiation.[63] Also, alizarin red S (ARS) staining was adopted to detect the production of extracellular calcium deposits during mineralization.[64] In this study, ALP activity and ARS staining had the highest degree in the UsCCP group (Figure 4B, C, and S15,16). The transcription levels of osteogenic genes on day 3 and 7 were presented in Figure 4D, and those of osteogenic genes in the UsCCP group were significantly increased compared with the Control and CMC/PASP groups. In brief, the immune microenvironment induced by UsCCP released from the scaffold promoted early osteoblast differentiation of mBMSCs, which was in line with previous findings that M2 macrophages could generate a favorable osteo-immunomodulatory microenvironment to promote osteogenesis.

Wound healing experiments and tube formation assays were performed to evaluate the effects of interaction between macrophages and biomaterials on angiogenesis.[65] Figure 4E visually illustrates the migration speed of cells from different groups, which is in the order of UsCCP > CMC/PASP > Control. Figure 4F shows a quantitative evaluation of cell migration, where a larger healing area

indicates better cell migration ability. The wound healing area rate of the UsCCP group was about 66.3%, which was significantly higher than that of other groups, implying that UsCCP group significantly enhanced the migration of HUVECs. After HUVECs cultured with different CMs for 24 h, RT-PCR was employed to investigate the expression of representative endothelial marker genes stromal cell-derived factor 1 (SDF-1) and von Willebrand factor (vWF) (Figure 4G). Compared with the Control group, the UsCCP group exhibited significant upregulation of both genes. Figure 4H demonstrates the optical microscope images of HUVEC cultured on Matrigel for 6 h under different CMs. Compared with the other groups, the UsCCP group had the largest number of nodes and junctions and a prominent tubular structure, reflecting a good tendency to form tubes. From the quantitative analysis presented in Figure 4I, the UsCCP group had the longest tubes and the largest number of branches. Thus, UsCCP released from the scaffold exhibited superior pro-angiogenic properties to the immune microenvironment of RAW264.7 cells and facilitated the angiogenesis of HUVECs *in vitro*.

2.5 Osteogenesis in vivo.

Based on the results of *in vitro* studies, rat skull defects were used to further evaluate the osteogenic ability of UsCCP scaffold. As for the number of animals, we originally selected 5 rats of each group at each time point for comparison. However, due to uncontrollable factors, including accidental death of some animals during post-operative feeding for individual animal differences and sample damage for improper sampling operations, there are only 3 valid data available for each group. In addition, after serious consideration of animal ethical issues and reference to many high-quality literatures using three animal samples for statistics (Nature Medicine[66], Science Immunology[67], Nature Communications[68], etc.), we finally decided to use 3 valid data of each group for statistical analysis in the manuscript. After 4 and 8 weeks into the experiment, micro-CT scanning was performed to

observe and analyze the regenerated bone. As depicted in Figure 5A, new bone was formed, the skull defect was partially healed, and the width of the skull defect in all groups was reduced at 4 weeks. In the defect, the newly formed bone tissue grew from the edge to the center. The defect center in the Control group and the CMC/PASP group was still clearly visible, while a large volume of new bones was observed in the defect center of the UsCCP group; therefore, the UsCCP group had better osteogenesis ability. By the 8 week, the defect in the UsCCP group was almost completely covered by new bone, and the new bone tissue was more continuous. Although the defect range in the Control group and the CMC/PASP group was lower than that in the 4 week, there was still a large gap between the experimental group. The ratio of bone surface area to tissue volume (BV/TV) and the average trabecular thickness (Tb.Th) of the UsCCP group were significantly higher than those of the other two groups (Figure 5B, D). Bone mineral density (BMD) is the main factor in evaluating the quality and strength of regenerated bone indicators. The results demonstrated that the bone density of the UsCCP group was the highest, reaching approximately 13 times that of the Control group after 8 weeks (Figure 5C).

Hematoxylin-eosin (H&E) and Masson's trichrome staining were performed to identify newly regenerated bone tissue and evaluate the *in vivo* osteogenic efficacy of UsCCP scaffolds in a rat critical-sized calvarial defect. The H&E staining (Figure 5E1, 2, 4, 5) detected more H&E red-stained areas in the defective areas treated with UsCCP scaffold compared with those in the other groups. Additionally, more small blood vessels were formed in the UsCCP group. This could help the new bone to differentiate from the original bone and make the cells in the defect area grow effectively. Masson's trichrome staining (Figure 5E3, 6) indicated the cartilage collagen (blue) and mature bone (red), where the darker red shows a more mature callus.

The *in vivo* biocompatibility of UsCCP scaffold was detected through serum biochemical indices, including alanine amino transferase (ALT), aspartate amino transferase (AST), alkaline phosphatase

(ALP), blood urea nitrogen (BUN), serum creatinine, and serum calcium. The UsCCP group presented no significant difference compared with the Control group, implying that the addition of materials did not cause major abnormalities in the liver and kidney function (Figure S17). Subcutaneous implantation was further studied to reveal the degradation of UsCCP scaffold *in vivo*. The UsCCP scaffold were implanted subcutaneously in rats (Figure S18A), and samples were collected on day 3, 7, and 14 (Figure S18B, C). After 3 days of implantation, the material was absorbed to a smaller extent, and a thick fibrous envelope was formed around it, with a considerable number of inflammatory cells. On day 7, the envelope was reduced, and inflammatory cells had infiltrated into the material. On day 14, almost all the material had been absorbed, leaving only small clumps of inflammatory cells.

2.6 Transcriptome sequencing analysis.

In order to examine the molecular mechanism of UsCCP scaffold, transcriptome sequencing analysis was conducted on cells cultured in different groups. All Pearson correlation values among samples were higher than 0.97, indicating good specimen stability (Figure S19). The Venn diagram of genetic variations (Figure S20) suggested many differences (1701) between the Control and UsCCP groups but only a slight discrepancy (233) in the Control and CMC/PASP groups. The volcano plot showed that, compared with the Control group, the number of significantly upregulated genes in macrophage cells cultured with UsCCP and CMC/PASP scaffold was 1099 and 86, while the number of downregulated genes was 602 and 147, respectively (Figure S21). Notably, there were many differences in gene expression between the UsCCP and CMC/PASP groups. The results suggested that UsCCP scaffold played a critical role in stimulating macrophages.

The 20 differential genes of the Control group vs. the UsCCP group were presented in Figure 6A, consisting of 17 upregulated genes and 3 downregulated genes. These genes play an essential role in cell proliferation, cell cycle, cell adhesion and migration, especially immune response, and

inflammation regulation. For instance, ornithine decarboxylase 1 (ODC1), associated with cell activation and proliferation, also inhibited inflammatory responses and ROS-induced apoptosis of macrophages.[69] The E26 avian leukemia oncogene 2,3' domain (EST2) inhibits inflammatory cytokines through the MAPK/NF-κB signaling pathway, and the elevated expression of EST promotes cell survival.[70] The C-type lectin domain family 4 member E (Clec4e) was shown to play a role in cell adhesion and intercellular signal transduction and activate macrophage functions *in vitro*.[71]

Next, GO term enrichment analysis was performed on the top 20 genes (Figure 6B, S22). Among these GO Terms of Biological Process, the performance of immune-related pathways was particularly prominent. As demonstrated by the top enriched up KEGG pathways (Figure 6C), many pathways were related to the immune system, including rheumatoid arthritis, graft-versus-host disease, IL-17 signaling pathway, C-type lectin receptor signaling pathway, T cell receptor signaling pathway, and allograft rejection. Moreover, the NF-kappa B signaling pathway and TNF signaling pathway significantly contributed to immuno-inflammatory responses. All differentially expressed genes in the inflammatory response and immune response were analyzed through the Gene Ontology (GO) database analysis. Five upregulated genes and five downregulated genes related to inflammatory response and immune response were illustrated in Figures 6D and E, respectively, presenting remarkable immune regulation and anti-inflammation trends. Figure 6F shows the genes related to the polarization of macrophages, indicating significant macrophage activation and polarization trend to the M2-type. Figure S23 depicts the Pearson's correlation of Figure 6D, E and F.

In brief, a safe and effective scaffold containing UsCCP was prepared to facilitate osteogenesis and vascularization by promoting intra-fibrous mineralization regulating macrophage polarization.

3. Conclusions

In this study, a simple method was employed to prepare a scaffold containing UsCCP. The scaffold could release the UsCCP at the bone defect site, adjust the calcium ion concentration in the bone

marrow microenvironment and change the pH value, then activate macrophages and facilitate the M2 type polarization of macrophages. Our experimental setup led to the formation of an immune microenvironment conducive to osteogenesis and angiogenesis. Besides, the UsCCP in the scaffold could penetrate the collagen fibers, enhance the mineralization of collagen fibers, and induce the same microstructure as natural mineralized fibers. This dynamic regulation of various biological functions plays a role in cells and the extracellular matrix, participates in all stages of bone healing, and promotes bone regeneration in the body. The biomaterial used in this study has a high application value; it demonstrates the potential of a new concept of synergistic and efficient regulation for the construction of bone tissue engineering.

4. Experimental Section

Synthesis of UsCCP

CMC and PASP were used as the matrix materials to prepare UsCCP. First, 0.2 mL of 1 M $CaCl_2$ (Aladdin, USA) solution was dropwise mixed with 0.15 mL of 0.3 g mL^{-1} PASP (Chengdu Aikeda Chemical Reagent Co., Ltd, China) solution. The mixed solution was slowly injected into 1 mL of 10% CMC (Nantong Feiyu Biological Technology Co., Ltd, China) solution with gentle stirring to obtain solution A. Next, 0.134 mL of 1 M Na_2HPO_4 (Aladdin, USA) solution was mixed with 1 mL 10% CMC solution and stirred to obtain solution B. Finally, solutions A and B were mixed and stirred until the solution was completely homogeneous, and the pH value was adjusted to 7.4 prior to use. The concentrations of calcium and phosphorus ion in the final dispersion were 80.5 mM and 53.9 mM, respectively. The UsCCP was frozen at -80°Cin advance for 2 h. Then, the sample was frozen in a vacuum freeze dryer for 24 h to produce the scaffold material. The controlled sample (CMC/PASP) was synthesized without the addition of $CaCl_2$ and Na_2HPO_4.

Characterization

A high-resolution transmission electron microscope (HRTEM, 2100F, Japan) was employed to examine the internal form of the material and observe the diameter of calcium phosphate nanocluster. The sample was dissolved in ethanol and diluted 100 times before each test. Mineral crystallinity was examined using selected area electron diffraction (SAED) with HRTEM. Scanning electron microscopy (SEM, GeminiSEM 300, Germany) with an EDS system was used to evaluate the microstructure of UsCCP scaffold with a 3 kV accelerating voltage, followed by coating with gold in an ion sputtering instrument. The porosity of UsCCP scaffold was calculated using image J. The sample was ground into powder, mixed with potassium bromide and underwent FTIR (IRAffinity-1, Shimadzu, Japan) scanning with 30 scans at 4 cm^{-1} resolution from 400 to 4000 cm^{-1} to examine the characteristic peak. The phase composition was analyzed by XRD (Bruker D8 ADVANCE, Bruker, Germany) with a 40 kV acceleration voltage and a 40 mA current. The diffraction intensity data were scanned from 10° to 70° in the 2θ range. The degradation of UsCCP scaffold was conducted in aseptic water. Briefly, 1 ml UsCCP was frozen in a vacuum freeze dryer for 24 h and weighed (W0). Each sample was then soaked in 2ml aseptic water and kept in cell incubator (37°Ç CO2 5%). The aseptic water was changed every other day. On day 1,3,5,7,10, five samples were taken out and stored at -80°Ceach time. Finally, all these samples were freeze-dried and then measured the residual mass (Wt). Degradation rate (%) = (W0 - Wt) / W0 x 100%. For compression test, scaffold was placed at the center of a couple of flat probes. Tests were conducted at a loading rate 2 mm/min and at room temperature. The compression modulus was calculated by the stress and strain within the elastic zone (1-3% strain). Five repeated tests were conducted to ensure the repeatability of experiments.

Collagen mineralization

First, preprocessed collagen solution was prepared as follows: 8.33 mL of 3 mg mL^{-1} type I collagen, rat tail (Gibco-Invitrogen, USA) was transferred into 0.5 mL assembly solution containing 50 mM

glycine solution and 200 mM potassium chloride, whose pH value was pre-adjusted to 9.2. The preprocessed collagen solution was dripped onto 300-mesh formvar/carbon coated nickel TEM grids and water-bathed overnight at 37°C. The TEM grids were immersed in 0.05% glutaraldehyde solution at 37°C for 1 h to cross-link the collagen. Then, they were soaked into the mineralizing solution of UsCCP, HAP at 37°C for 1h, 12 h and 24 h. After mineralization, the TEM grids were taken out, and gradient elution was performed sequentially with deionized water, 50% ethanol and 100% ethanol. Finally, the mineralization of collagen was observed by HRTEM (JEM2100F, Japan). The lattice fringe of the mineral in mineralized collagen fibril was calculated by Gatan Microscopy Suite Software.

For the STORM experiment, the laser confocal culture dish (LCCD) was amino-silanized with aminopropyltriethoxysilane (APTES) for 2 h to immobilize collagen fibrils, washed with anhydrous ethanol and deionized water, and oven-dried before use. The preprocessed collagen solution was dripped onto the APTES-modified LCCD glass, incubated at 37°C for 12 h, and added with 0.05 wt% glutaraldehyde to further cross-link collagen fibrils for 1 h. Before mineralization, the type I collagen fibrils were labeled by immunofluorescent staining. The collagen fibrils were incubated with type I collagen rabbit anti-mouse antibody (1:200, Abcam, USA) at 4°C overnight and then colored with mouse anti-rabbit 594 secondary antibodies (1:500, Abcam, USA) for 1 h at room temperature. The UsCCP scaffold was used to mineralize collagen fibers at 37°C for 24 h, and 10 μmol calcein AM (BestBio, shanghai, China) was employed to label the mineralized collagens. The samples were immersed in an imaging buffer and observed through a Nikon Ti-E inverted optical microscope (N-STORM/A1R, Japan). After taking STORM images, the reconstruction of each 3D super-resolution image was performed with Nikon NIS Elements 4.30 software.

Ion concentration and pH test

RAW 264.7 cells were co-cultured with UsCCP and CMC/PASP scaffold through transwell migration assay (Figure 3A) to detect the concentrations of calcium and phosphorus ion. At each time point,

the culture medium was collected, and the ion release was tested by ICP-MS (Agilent7800, USA). For the assessment of pH variation, the culture medium was measured with a pH meter (METTLER TOLEDO, FiveEasy Plus) to obtain the pH value at 1, 2, 3, and 4 days.

Cell culture

In this work, the murine macrophage-like cell line RAW264.7 (the Cell Bank of the Chinese Academy of Sciences of Shanghai) was adopted for macrophage experiments. The cells were cultured in Dulbecco's modified Eagle's medium (DMEM) supplemented with 10% fetal bovine serum (FBS, Gibco, USA) and 1% penicillin/streptomycin (Sigma, USA) at 37°C in a 5% CO_2 atmosphere. Cells were routinely passaged every third day. HUVECs (ATCC, USA) were cultured in an endothelial cell medium (ECM, Sciencell, USA) with 5% FBS and 1% endothelial cell growth supplement/heparin kit (ECGS/H, Promocell). Four-week-old male C57BL/6J mice were adopted to extract mBMSCs according to previous reports.[72] Fluorescent staining was performed to identify mBMSCs through CD45-APC, CD90-PE, CD29-FITC (eBioscience), and CD34-FITC (BioLegend).

Macrophage response

RAW264.7 cells were co-cultured with UsCCP or CMC/PASP scaffold through transwell migration assay (Corning, USA), and the cells cultured in a normal medium were used as the Control group. CCK-8 assay and live/dead assay were utilized to evaluate the cytocompatibility for 1, 2 and 3 days in accordance with the instructions. The live and dead cell numbers were calculated by Image J (National Institute of Health). Each group contained three replicates. To analyze the effect of UsCCP on cell morphology, the cell cytoskeleton was observed. After being co-cultured with three different groups for 1 and 2 days, the cells were stained with 70 nmol rhodamine-phalloidin (Cytoskeleton Inc, USA) and 5 μg/mL DAPI (Solarbio, Beijing, China). Subsequently, confocal laser scanning microscopy (CLSM, Leica Microsystems, German) was used to take photographs.

The expression of CD11c (M1 marker) or CD206 (M2 marker) in Raw 264.7 cells were detected by flow cytometry. After 1 and 2 days of co-culture, the cells were stained with Fixable Viability Stain 520 (BD Pharmingen, USA), the Fc-receptors were blocked with purified rat anti-mouse CD16/CD32 (BD Pharmingen, USA), then labeled with PE-conjugated anti-mouse CD163 (BD Pharmingen, USA) and PE-cy7-conjugated anti-mouse CD11c antibodies (BD Pharmingen, USA) for 1 h in the dark. Next, cells were assayed with a flow cytometer (BD Biosciences Pharmingen, CytoFLEX LX, USA), and the data were analyzed with Flowjo software.

Macrophage polarization was studied through the immunofluorescence staining assay. For the staining step, IL-1R1 (1:100, Santa Cruz Biotechnology, USA) was used as a pro-inflammatory marker, and Arg-1 (1:50, CST, USA) was adopted as an anti-inflammatory marker. After being cultured with different materials for 1 and 2 days, the cells were incubated with primary antibodies at 4°C overnight. Subsequently, the secondary antibodies goat anti-rabbit Alexa Fluor 594 and goat anti-mouse Alexa Fluor 488 (1:500, Abcam, USA) were incubated with the cells at room temperature for 1 h. Images were taken with confocal laser scanning microscope. The fluorescent density of images was quantified by Image J software.

The relative gene expression levels of macrophages cultured in different groups were investigated by real-time PCR assays. After 1 and 2 days of incubation, total cell RNA was extracted using the TRIZOL reagent (Invitrogen) and reverse-transcribed to cDNA by means of a PrimeScript RT reagent kit (Takara Bio, Japan) following the manufacturers' instructions. Specific gene primers for TNF-α, IL-6, IL-1β1, INOS, IL-10, Arg-1, IL-4, IL-1Ra, CD86, CD206, BMP2, VEGF, PDGF-BB, and GAPDH were commercially synthesized (Sangon Biotech Co., Ltd, China). The specific primer sets are listed in Table S1. Quantitative real-time PCR analysis was performed with a mixture of BioEasy SYBR Green I, cDNA templates and primers. All mRNA values were normalized against GAPDH expression using the comparison Ct ($2^{-\Delta\Delta Ct}$) method.

After 1 and 2 days of co-culture, the Arg-1 and INOS proteins levels of three groups were measured by western blot using antibodies including rabbit-anti-arginase-1 (CST, USA, 1:1000), rabbit-anti-INOS (HuaAn Biotechnology Co., Ltd., China, 1:1000), and anti-GAPDH (Proteintech, USA, 1:1000). The protein was separated on sodium dodecyl sulfate-polyacrylamide electrophoresis gel, transferred onto PVDF membrane (Millipore, USA), incubated with primary antibodies overnight at 4°C, then incubated with a horseradish peroxidase-conjugated secondary antibody (1:10000) at room temperature for 1 h. The immunocomplexes were visualized by ECL chemiluminescence (NCM Biotech, Suzhou, China). All proteins were normalized to the value of GAPDH. The relative integrated density of protein bands was analyzed by Image J.

Collection and preparation of CM

Raw 264.7 cells were co-cultured with different groups for 2 days. Then, the culture medium of the respective groups was collected and centrifuged at 1500 rpm for 15 min at 4°C. The filtered supernatants were mixed with a complete culture medium at the ratio of 1:2 to obtain conditioned medium (CM). Subsequently, the osteogenic-inducing medium was prepared. Moreover, mBMSCs and HUVECs were cultured on plates in a complete medium in a 5% CO_2 incubator at 37°C for 24 h. Next, the culture medium was changed into different CMs to examine cell proliferation and the osteogenic and angiogenic ability of CM. The culture medium was refreshed every 2 days during the experimental period.

Expression of osteogenesis/angiogenesis-related genes

The mBMSCs and HUVECs were plated on 6-well plates. After 24 h of incubation, the culture medium was replaced by osteogenic-inducing CM. On days 3 and 7, total RNA from cells in different groups was extracted by TRIZOL. The expression levels of mouse mRNA encoding genes were detected for ALP, OPN, COL I, OSX, OCN, Runx2, SDF-1, and vWw, with the housekeeping gene GAPDH as the internal control.

After 3 and 7 days of cultivation in osteogenic-inducing CM, cells were stained with the BCIP/NBT ALP Color Development Kit (Beyotime, China). Furthermore, the ALP activity of mBMSCs was measured with an ALP activity kit (LabAssay™, Japan) and quantified by their OD values. On day 14 after osteogenic induction, ARS staining (Solarbio, China) was performed to examine the extracellular matrix mineralization of mBMSCs stimulated by CM. For quantitative results, 10% cetylpyridinium chloride (CPC; Sigma-Aldrich, USA) was added to dissolve mineralized nodules, and the absorbance of the solutions at 570 nm was measured using a microplate reader.

HUVECs were seeded in a 12-well plate. After the cells reached 100% confluence, monolayer HUVECs were carefully scratched with 10 µL pipette tips and the medium was replaced with the CM. Images were taken using an optical microscope after incubation for 8 h. The area percentage of wound healing was calculated by Image J software.

A tubule-forming experiment was performed to evaluate the angiogenesis ability of different CMs.[73] Briefly, 50 µL Matrigel™ (BD, USA) was added to a 96-well plate and incubated at 37°C for 30 min for matrigel gelatinization. Then, HUVECs suspended with different CM were inoculated to the gel and images were taken by an optical microscope after 6 h of incubation. Six images were analyzed by Image J software for respective groups.[74] The number of new tubes, total branching points and length of the total tube were calculated for the quantitative analysis of angiogenesis.

Rat subcutaneous implantation experiment

Eight male Sprague Dawley rats (4 weeks, 100-120 g) were anesthetized, and the dorsal hair was shaved. Then, two independent subcutaneous incisions were created on the back of each rat, and UsCCP scaffold was implanted. Each scaffold had the same size. Rats were euthanized by CO_2 asphyxiation after 3, 7 and 14 days of implantation. The dorsal tissue was harvested, trimmed, fixed, processed into paraffin blocks, and sectioned into 4 µm thickness. According to standard procedures, the sections were deparaffinized, hydrated, and stained with hematoxylin and eosin.

Rat calvarial bone defect model

In order to examine the effects of UsCCP scaffold on regeneration of new bone in bone defects, a total of 20 male Sprague Dawley rats (8 weeks, 220-250 g) were randomly divided into two groups (UsCCP group, CMC/PASP group). After being anesthetized, 5 mm-sized critical calvarial defects were constructed on two sides of the mediocranial suture with a trephine bur.[75] All the defects on the left side were used as the blank group, and the defects on the right side were implanted with UsCCP or CMC/PASP scaffold. After post-operation for 4 and 8 weeks , the samples were harvested and subjected to osteogenesis evaluation.

All animal experimental procedures were approved by the Medical Ethics Committee of Zhejiang University (approval number: ZJU20200126).

Micro-CT analysis and histological evaluation

After 4 and 8 weeks, the rats were euthanized. The calvarial tissues were harvested and soaked in 10% neutral buffered formalin for 24 h for osteogenesis evaluation. The Micro-CT system (MILabs U-CT-XUHR, Netherlands) was used to analyze some changes in the skull. Scanning was performed with a resolution of 20 µm, and the projections were acquired at the angle of 360°. Micro-CT images were acquired at 80 keV and 500 mA. The data were put into the IMALYTICS Preclinical software for reconstruction and analysis. A 5-mm diameter round-shaped region of interest (ROI) around the epicenter of the defect was analyzed. After setting a determinate threshold, the new bone volume fraction (BV/TV), bone mineral density (BMD) and thickness (Tb. Th) in the defect site were calculated directly on 3D images of the specimen.All samples were decalcified with 5% ethylenediaminetetraacetic acid (EDTA) for two months. Then, samples were dehydrated, embedded in paraffin and cut into 5 µm sections. These were stained with hematoxylin and eosin (H&E, Solario) and Masson's trichrome (Solario) separately, and observed using an Olympus VS200 to evaluate the formation of new bone.

After surgery for 4 and 8 weeks, the blood for different groups was collected for liver and kidney function tests. The blood biochemical parameters were measured with an automatic biochemical analyzer (Wuhan servicebio technology CO., LTD), including alanine amino transferase (ALT), aspartate amino transferase (AST), alkaline phosphatase (ALP), blood urea nitrogen (BUN), serum creatinine, and serum calcium.

Transcriptome analysis

The cells were subjected to transcriptome analysis at 2 days. Briefly, the cells were treated with TRIZOL for the extraction of total RNA, then eukaryotic mRNA was enriched by Oligo(dT) beads and reverse transcribed into cDNA. Next, the cDNA fragments were purified and amplified. FPKM (fragment per kilobase of transcript per million mapped reads) value of each gene was calculated to quantify its expression abundance and variations using StringTie software. The DEGs, GO (gene ontology) and KEGG (Kyoto Encyclopedia of Genes and Genomes) enrichment analyses were performed using R software. The false discovery rate (FDR) < 0.05 and absolute fold change ≥ 2 were set as the thresholds for significantly differential expression or differential enrichment.

Statistical analysis

All experiments were conducted in triplicate, and the results were presented as mean ± standard deviation (SD). Prism Software version 8.01 (GraphPad) was used for the statistical analysis. One-way analysis of variance (ANOVA) followed by Tukey's post-hoc test were performed to determine statistical significance. $P < 0.05$ and $p < 0.01$ indicated significance and high significance, respectively.

Ackonwledgements

This research was supported by Zhejiang Province key research and development program(2021C03059) and the Nation Key R&D program of China (2018YFC1105101). The authors

wish to thank Chao Bi, Xiaoli Hong and Wei Yin at the Core Facilities of Institute of Translational Medicine, Zhejiang University School of Medicine for technical assistance in flow cytometry, confocal microscopy and STORM microscopy.

Conflict of Interest

The authors declare no conflict of interest.

Author Contributions

Jue Shi and Zhijian Xie supervised the project. Ruikang Tang conceived and designed the experiments. Yanyan Zhou and Zihe Hu performed all experiments and wrote the paper. All authors analyzed and discussed the data. Wenjing Jin and Changyu Shao revised the manuscript together with Jue Shi and Zhijian Xie.

Supporting Information

Supporting Information is available from the Wiley Online Library or from the author.

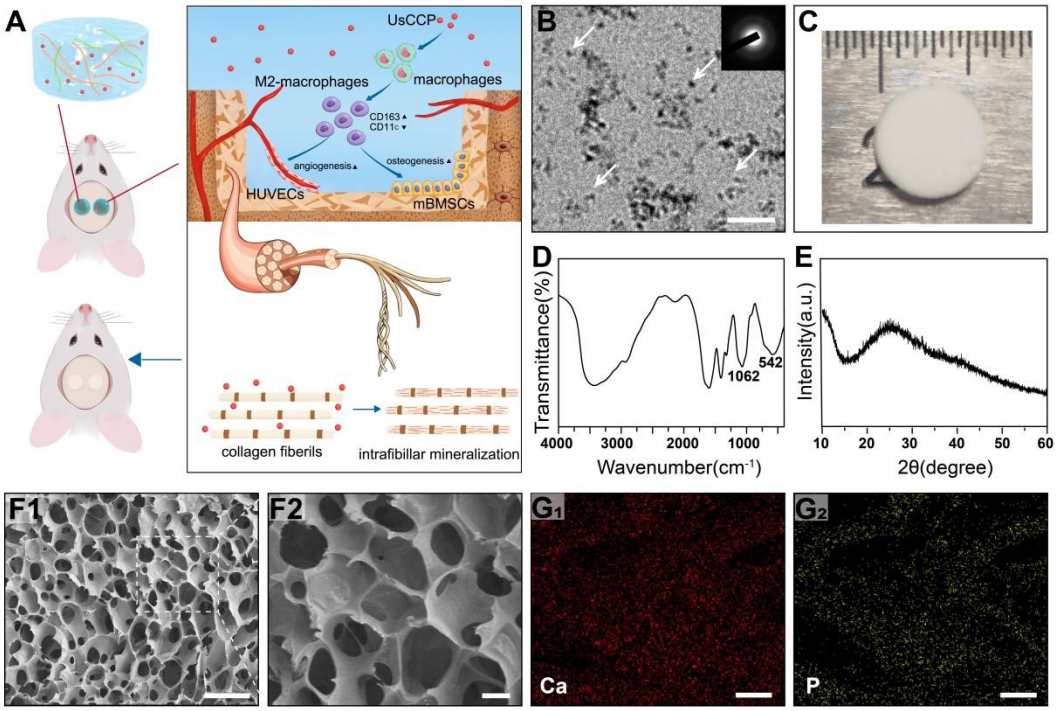

Figure 1: The characteristics of UsCCP. (A) Schematic illustration of this experiment. (B) TEM image and SAED pattern (inset) of UsCCP, scale bar: 20nm. (C) Digital photograph of UsCCP scaffold. (D) FTIR spectra of UsCCP scaffold. (E) XRD analysis of UsCCP scaffold. (F1) The SEM image of UsCCP scaffold, scale bar: 100 µm. (F2) Local magnified SEM image of (F1), scale bar: 25 µm. EDS mapping images of UsCCP scaffold, (G1) calcium , (G2) phosphorus, scale bar: 25µm.

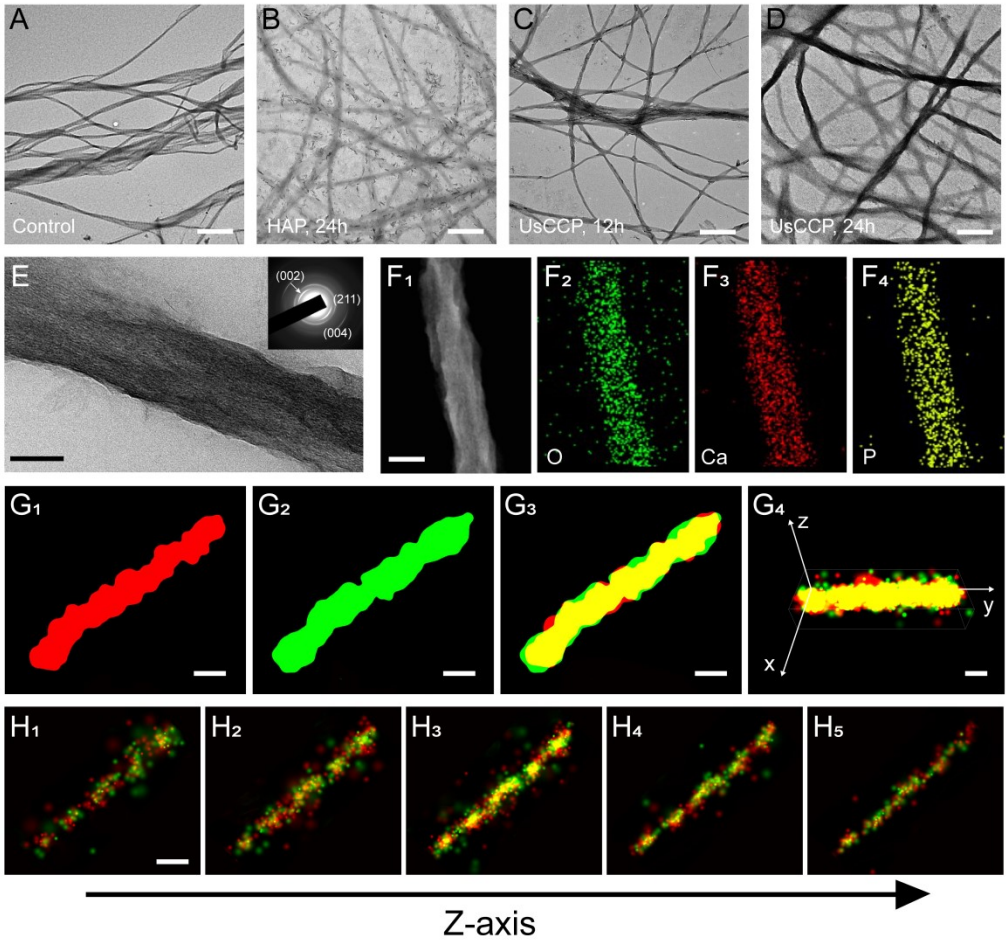

Figure 2: Effect of UsCCP to mineralization process of collagen mineralization. (A) TEM image of the native collagen fibrils. (B)TEM image of collagen fibrils after incubated with HAP at 37℃ for 24h. (C, D) TEM images of collagen fibrils after incubated with UsCCP scaffold at different time points at 37℃C) 12h, D) 24h. (E) A local magnified image of D (inset shows SAED patterns of collagen fibrils). (F) EDS mapping images of collagen fibrils in E: oxygen (F2), calcium (F3) and phosphorus (F4). (G) The xy projections of STORM images of mineralized collagen fibrils in the UsCCP group at 24h. G1) collagen fibrils were labeled with Alexa Fluor 594 dye (red fluorescence); G2) HAP was labeled with calcein (green fluorescence); G3) merge image of G1 and G2. G4) 3D STORM image of the mineralized collagen fibrils in the UsCCP group at 24h. (H) Z-slice of STORM images of the mineralized collagen fibrils in the UsCCP group at 24h. Scale bar: 1 μm (A-D), 100 nm (E-H).

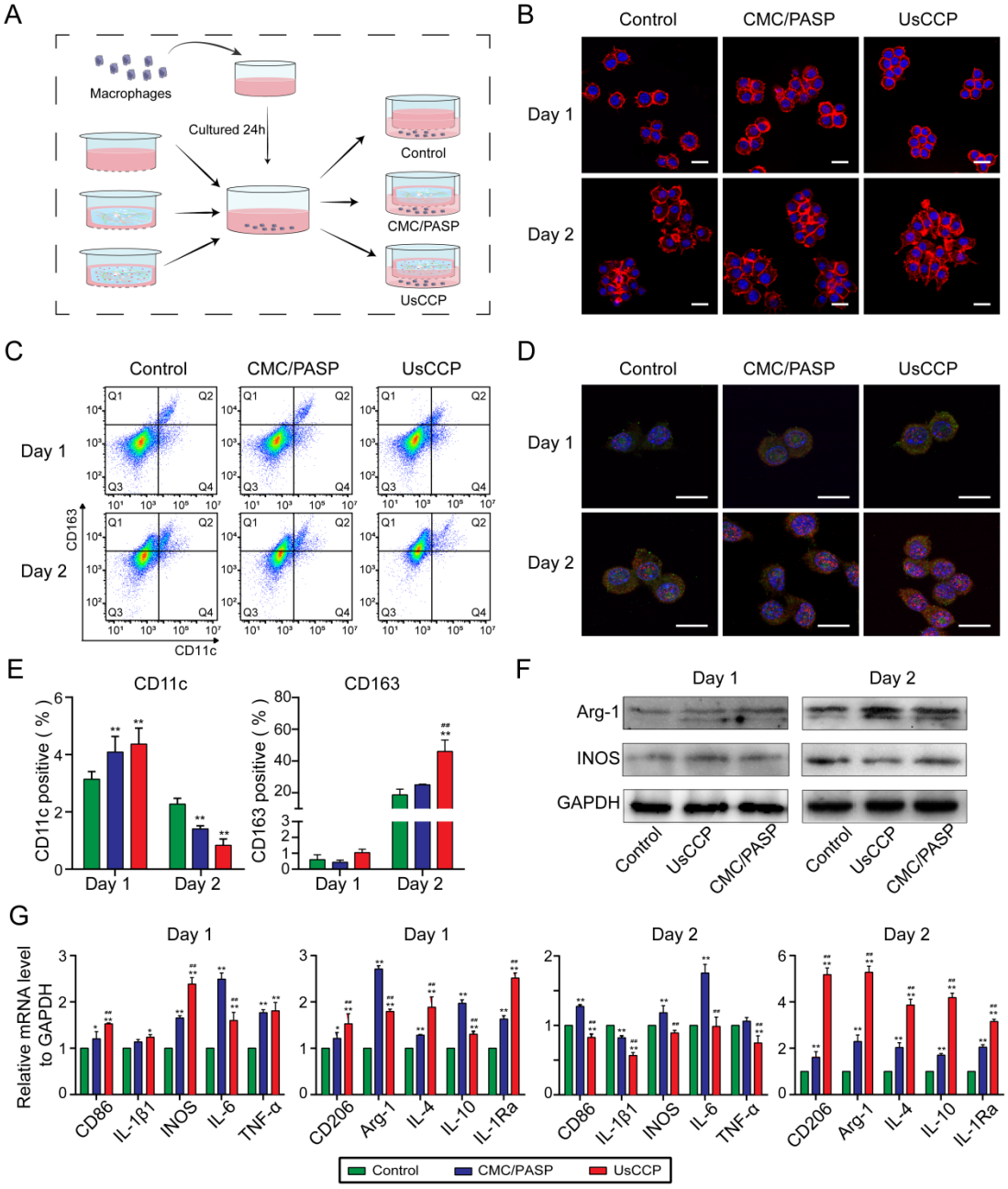

Figure 3: The response of RAW264.7 cells cultured with UsCCP scaffold. (A) Schema of co-culture of cell and materials. (B) Phalloidin staining was performed to observe the morphology of RAW264.7 cells on day 1 and 2. DAPI: blue, Phalloidin: red. Scale bar: 20 µm. (C)The scatter plot of flow cytometry detection of M1 and M2 macrophage surface markers CD11c and CD163. (D) Representative pictures of Arg-1 (red) and IL-1R1 (green) immunofluorescence staining of Raw 264.7 cells after UsCCP treatment for day 1 and 2. Scale bar: 20µm. (E) Mean Fluorescence Intensity (MFI) of CD163 and CD11c in the three groups. (F) The protein expression of Agr-1 and INOS was

determined by Western blot analysis. (G) RT-PCR detection of pro-inflammatory and anti-inflammatory related genes of different groups in macrophages cultured for day 1 and 2. Data representthe mean ± S.D. (n = 3). Significant differenceswere derived from ANOVA followed by Tukey's post hoc test: *, # P < 0.05, **, ## P < 0.01, * represents comparison with Control group, # represents comparison with CMC/PASP group.

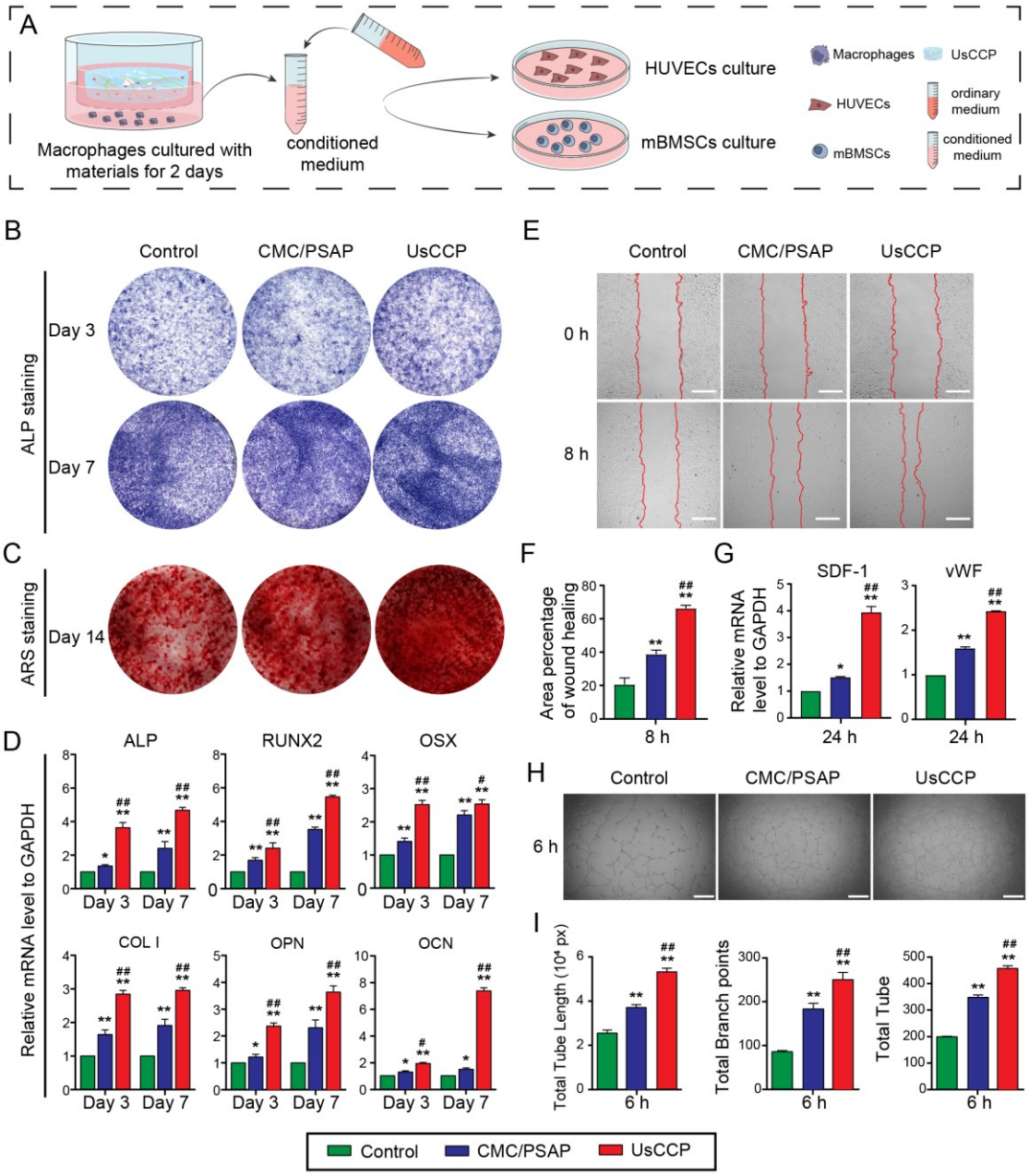

Figure 4: The influences of biomaterial-mediated immunomodulatory effects on the osteogenic differentiation of mBMSCs and angiogenesis of HUVECs in vitro. (A) Schema of conditioned medium

preparation and cell culture (B) ALP staining after incubated for 3 and 7 days. (C) ARS staining after incubated for 14 days. (D) The mRNA expression of osteogenesis-related genes was analyzed after incubated for 3 and 7 days. (E) Representative images of cell migration of HUVECs, Scale bar: 200µm. (F) The percentage of coverage after 8h of wound healing; (G) The relative gene expressions of SDF-1 and vWF in HUVECs after incubated for 24h. (H) Representative images of tube formation for 6h, Scale bar: 200 µm. (I) Quantitative analysis of total tube length, total branch points and total tubes points per field. Data representthe mean ± S.D. (n = 3). Significant differenceswere derived from ANOVA followed by Tukey's post hoc test: *, # $P < 0.05$, **, ## $P < 0.01$, * represents comparison with Control group, # represents comparison with CMC/PASP group.

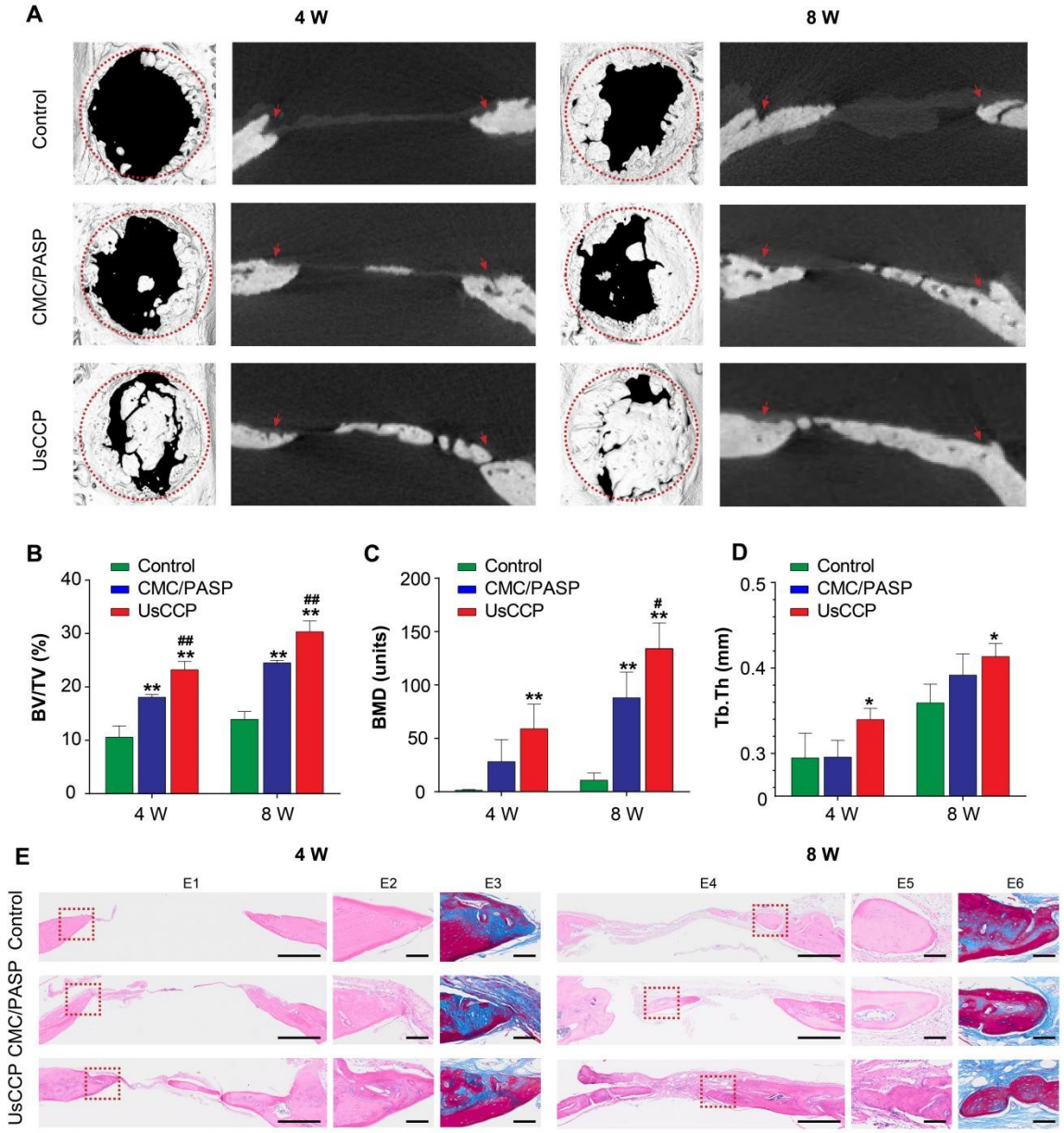

Figure 5: In vivo osteogenesis ability of UsCCP scaffold in rat calvarial defect for 4 and 8 weeks. (A) The micro-CT images of the bone defect. (B-D) The quantitative analysis of micro-CT: B) BV/TV; C) BMD, D) Tb.Th. (E) H&E and Masson staining of the defect area after implanted, Scale bar: 500 µm (E1, E4), 100 µm (E2, E3, E5, E6). Data representthe mean ± S.D. (n = 3). Significant differenceswere derived from ANOVA followed by Tukey's post hoc test: *, # P < 0.05, **, ## P < 0.01, * represents comparison with Control group, # represents comparison with CMC/PASP group.

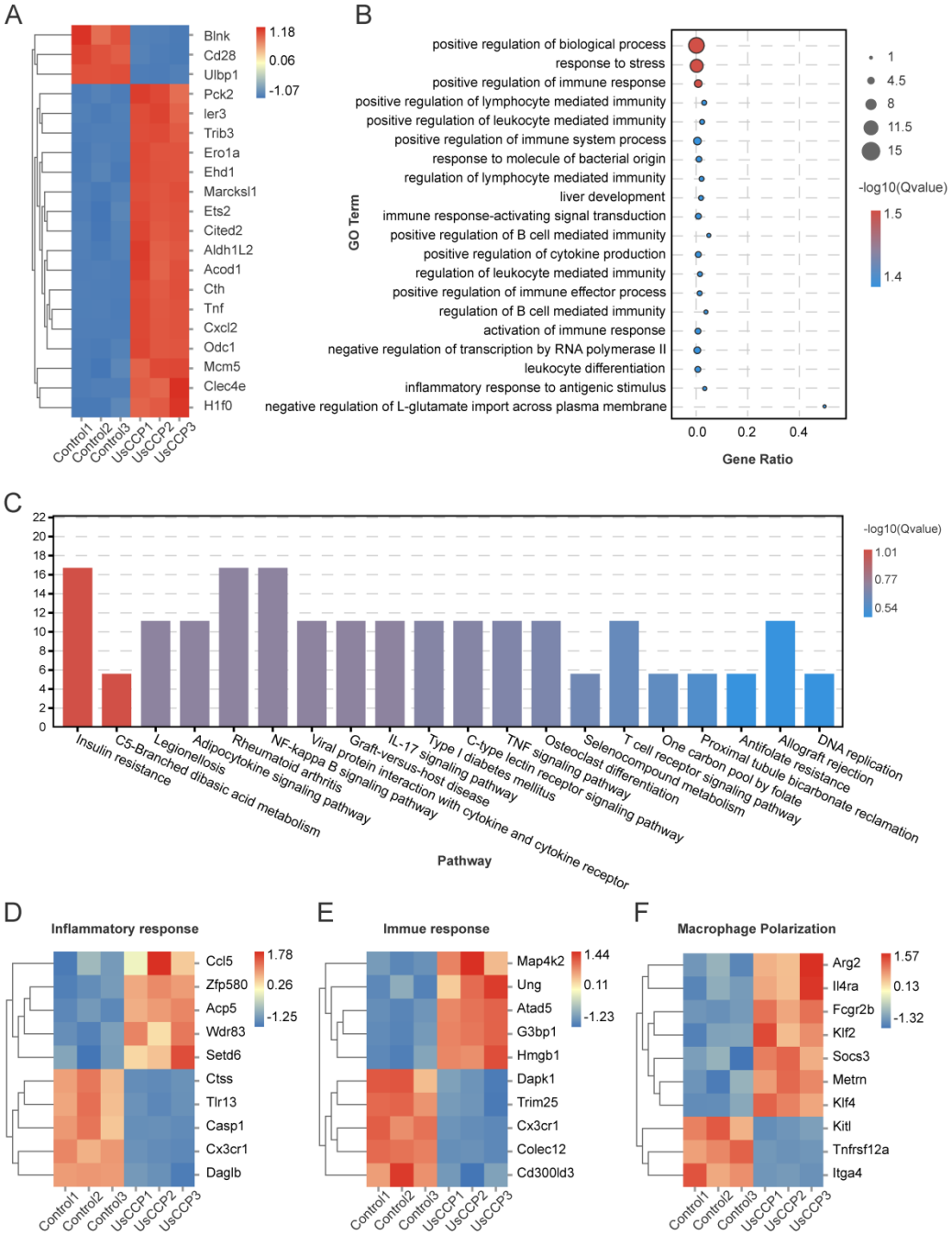

Figure 6: Bioinformatic analysis of macrophage gene expression of different samples. (A) Heatmap of the top 20 differential genes of Control vs UsCCP group. (B) Analysis of the top 20 enriched terms of Biological Process by GO pathways for the top 20 genes. (C) Analysis of the top 20 enriched terms by KEGG pathways for the top 20 genes. (D) Heatmap from the inflammatory response pathway in Control and UsCCP groups. (E) Heatmaps from the immune response pathway in Control and UsCCP

groups. (F) Heatmaps of differentially expressed genes with macrophage polarization in Control and UsCCP groups. n = 3 per group

Reference

[1] Q. Wang, J. Yan, J. Yang, B. Li, *Materials today* **2016**, 19, 451.

[2] K. Zhou, P. Yu, X. Shi, T. Ling, W. Zeng, A. Chen, W. Yang, Z. Zhou, *ACS Nano* **2019**, 13, 9595.

[3] F. Yu, R. Lian, L. Liu, T. Liu, C. Bi, K. Hong, S. Zhang, J. Ren, H. Wang, N. Ouyang, L. Du, Y. Liu, L. Zhou, Y. Liu, B. Fang, Y. Li, S. Duan, L. Xia, *ACS Nano* **2022**, 16, 755.

[4] S. Pina, J. M. Oliveira, R. L. Reis, *Advanced Materials* **2015**, 27, 1143.

[5] M. Zhang, R. Lin, X. Wang, J. Xue, C. Deng, C. Feng, H. Zhuang, J. Ma, C. Qin, L. Wan, J. Chang, C. Wu, *Science advances* **2020**, 6, 6725.

[6] L. Yu, D. W. Rowe, I. P. Perera, J. Zhang, S. L. Suib, X. Xin, M. Wei, *ACS Applied Materials & Interfaces* **2020**, 12, 18235.

[7] J. Wang, Q. Liu, Z. Guo, H. Pan, Z. Liu, R. Tang, *ACS Biomaterials Science & Engineering* **2021**.

[8] O. A. Tertuliano, J. R. Greer, *Nature Materials* **2016**, 15, 1195.

[9] Y. Wang, T. Azaïs, M. Robin, A. Vallée, C. Catania, P. Legriel, G. Pehau-Arnaudet, F. Babonneau, M. Giraud-Guille, N. Nassif, *Nature Materials* **2012**, 11, 724.

[10] J. Zhang, B. Zhang, Z. Zheng, Q. Cai, J. Wang, Q. Shu, L. Wang, *Advanced Functional Materials* **2022**, 32, 2109882.

[11] S. Yao, B. Jin, Z. Liu, C. Shao, R. Zhao, X. Wang, R. Tang, *Advanced Materials* **2017**, 29, 1605903.

[12] A. Dey, P. H. H. Bomans, F. A. Müller, J. Will, P. M. Frederik, G. de With, N. A. J. M. Sommerdijk, *Nature Materials* **2010**, 9, 1010.

[13] F. Nudelman, K. Pieterse, A. George, P. H. H. Bomans, H. Friedrich, L. J. Brylka, P. A. J. Hilbers, G. de With, N. A. J. M. Sommerdijk, *Nature Materials* **2010**, 9, 1004.

[14] A. Lotsari, A. K. Rajasekharan, M. Halvarsson, M. Andersson, *Nature Communications* **2018**, 9, 4170.

[15] R. Gelli, F. Ridi, P. Baglioni, *Advances in Colloid and Interface Science* **2019**, 269, 219.

[16] P. Wang, L. Zhao, J. Liu, M. D. Weir, X. Zhou, H. H. K. Xu, *Bone Research* **2014**, 2, 14017.

[17] C. J. S. Ibsen, D. Chernyshov, H. Birkedal, *Chemistry - A European Journal* **2016**, 22, 12347.

[18] D. de Melo Pereira, P. Habibovic, *Advanced Healthcare Materials* **2018**, 7, 1800700.

[19] Q. Zhou, M. Guo, Q. Zhang, Q. Li, C. Y. Cao, *Materials & Design* **2021**, 210, 110093.

[20] Z. Chen, S. Cao, H. Wang, Y. Li, A. Kishen, X. Deng, X. Yang, Y. Wang, C. Cong, H. Wang, X. Zhang, *PLOS ONE* **2015**, 10, e116553.

[21] S. Yao, X. Lin, Y. Xu, Y. Chen, P. Qiu, C. Shao, B. Jin, Z. Mu, N. A. J. M. Sommerdijk, R. Tang, *Advanced Science* **2019**, 6, 1900683.

[22] S. Dorozhkin, *Materials* **2009**, 2, 1975.

[23] X. Zhang, Y. Wang, N. Manh, H. Wang, X. Zhong, C. Li, *International Journal of Nanomedicine* **2016**, 11, 2053.

[24] T. Yang, P. Xie, Z. Wu, Y. Liao, W. Chen, Z. Hao, Y. Wang, Z. Zhu, W. Teng, *Frontiers in Bioengineering and Biotechnology* **2020**, 8.

[25] S. Kim, K. Kim, B. S. Kim, Y. An, U. Lee, S. Lee, S. L. Kim, B. Kim, N. S. Hwang, *Biomaterials* **2020**, 242, 119905.

[26] B. Cai, D. Lin, Y. Li, L. Wang, J. Xie, T. Dai, F. Liu, M. Tang, L. Tian, Y. Yuan, L. Kong, S. G. F. Shen, *Advanced Science* **2021**, 8, 2100584.

[27] H. M. Rostam, L. E. Fisher, A. L. Hook, L. Burroughs, J. C. Luckett, G. P. Figueredo, C. Mbadugha, A. C. K. Teo, A. Latif, L. Kämmerling, M. Day, K. Lawler, D. Barrett, S. Elsheikh, M. Ilyas, D. A. Winkler, M. R. Alexander, A. M. Ghaemmaghami, *Matter* **2020**, 2, 1564.

[28] D. R. Griffin, M. M. Archang, C. Kuan, W. M. Weaver, J. S. Weinstein, A. C. Feng, A. Ruccia, E. Sideris, V. Ragkousis, J. Koh, M. V. Plikus, D. Di Carlo, T. Segura, P. O. Scumpia, *Nature Materials* **2021**, 20, 560.

[29] N. Jain, V. Vogel, *Nature Materials* **2018**, 17, 1134.

[30] J. Wang, X. Chen, X. Yang, B. Guo, D. Li, X. Zhu, X. Zhang, *Journal of Biomedical Materials Research Part A* **2020**, 108, 1305.

[31] G. Feng, C. Qin, X. Yi, J. Xia, J. Chen, X. Chen, T. Chen, X. Jiang, *Journal of Materials Science: Materials in Medicine* **2018**, 29.

[32] X. Chen, M. Wang, F. Chen, J. Wang, X. Li, J. Liang, Y. Fan, Y. Xiao, X. Zhang, *Acta Biomaterialia* **2020**, 103, 318.

[33] G. Balasundaram, M. Sato, T. J. Webster, *Biomaterials* **2006**, 27, 2798.

[34] W. E. G. Müller, M. Ackermann, B. Al-Nawas, L. A. R. Righesso, R. Muñoz-Espí, E. Tolba, M. Neufurth, H. C. Schröder, X. Wang, *Acta Biomaterialia* **2020**, 118, 233.

[35] L. Chen, P. Qiao, H. Liu, L. Shao, *Inflammation* **2021**, 44, 278.

[36] S. Heng, Z. Lu, Q. Liu, T. Jiang, M. He, F. Song, J. Zhao, L. Zheng, *Materials Science and Engineering: C* **2020**, 110, 110691.

[37] S. K. Bhadada, S. D. Rao, *Calcified Tissue International* **2021**, 108, 32.

[38] C. Shao, R. Zhao, S. Jiang, S. Yao, Z. Wu, B. Jin, Y. Yang, H. Pan, R. Tang, *Advanced Materials* **2018**, 30, 1704876.

[39] S. Kalliola, E. Repo, V. Srivastava, J. P. Heiskanen, J. A. Sirviö, H. Liimatainen, M. Sillanpää, *Colloids and Surfaces B: Biointerfaces* **2017**, 153, 229.

[40] J. Jin, Z. Ji, M. Xu, C. Liu, X. Ye, W. Zhang, S. Li, D. Wang, W. Zhang, J. Chen, F. Ye, Z. Lv, *ACS Biomaterials Science & Engineering* **2018**, 4, 2541.

[41] X. Zhao, L. Zhou, Q. Li, Q. Zou, C. Du, Carbohydrate Polymers 2018, 195, 225.

[42] D. Hu, Q. Ren, Z. Li, L. Zhang, *Molecules* **2020**, 25, 4785.

[43] M. Sarem, S. Lüdeke, R. Thomann, P. Salavei, Z. Zou, W. Habraken, A. Masic, V. P. Shastri, *Advanced Materials* **2017**, 29, 1701629.

[44] X. Li, C. A. van Blitterswijk, Q. Feng, F. Cui, F. Watari, Biomaterials 2008, 29, 3306.

[45] Z. Zhao, R. Fang, Q. Rong, M. Liu, *Advanced Materials* **2017**, 29, 1703045.

[46] W. He, A. K. Rajasekharan, A. R. Tehrani-Bagha, M. Andersson, *Advanced Materials* **2015**, 27, 2260.

[47] B. Cantaert, E. Beniash, F. C. Meldrum, *Chemistry* **2013**, 19, 14918.

[48] P. Wang, L. Zhao, J. Liu, M. D. Weir, X. Zhou, H. H. Xu, Bone Res **2014**, 2, 14017.

[49] H. He, C. Shao, Z. Mu, C. Mao, J. Sun, C. Chen, R. Tang, X. Gu, *Carbohydr Polym* **2020**, 229, 115547.

[50] P. Qiu, M. Li, K. Chen, B. Fang, P. Chen, Z. Tang, X. Lin, S. Fan, *Biomaterials* **2020**, 227, 119552.

[51] M. Li, X. Chu, D. Wang, L. Jian, L. Liu, M. Yao, D. Zhang, Y. Zheng, X. Liu, Y. Zhang, F. Peng, *Biomaterials* **2022**, 282, 121408.

[52] C. Combes, C. Rey, *Acta Biomaterialia* **2010**, 6, 3362.

[53] S. Allegrini, A. C. Da Silva, M. Tsujita, M. B. Salles, S. A. Gehrke, F. J. C. Braga, *Microscopy Research and Technique* **2018**, 81, 579.

[54] S. Ali Akbari Ghavimi, B. N. Allen, J. L. Stromsdorfer, J. S. Kramer, X. Li, B. D. Ulery, *Biomedical Materials* **2018**, 13, 55005.

[55] P. W. Andreotta, S. Arold, J. Kenyon, D. Spicer, P. Woodman, E. Berry, T. Brogan, S. Kong, P. Okerholm, V. Russell, R. W. Clarke, D. L. Hava, *Pulmonary Pharmacology & Therapeutics* **2018**, 53, 86.

[56] H. Wu, Y. Yin, X. Hu, C. Peng, Y. Liu, Q. Li, W. Huang, Q. Huang, *ACS Biomaterials Science & Engineering* **2019**, 5, 5548.

[57] K. Li, L. Lv, D. Shao, Y. Xie, Y. Cao, X. Zheng, *Journal of Functional Biomaterials* **2022**, 13, 31.

[58] T. U. Luu, S. C. Gott, B. W. Woo, M. P. Rao, W. F. Liu, *ACS Appl Mater Interfaces* **2015**, 7, 28665.

[59] F. Y. Mcwhorter, T. Wang, P. Nguyen, T. Chung, W. F. Liu, *Proc Natl Acad Sci U S A* **2013**, 110, 17253.

[60] C. Guder, S. Gravius, C. Burger, D. C. Wirtz, F. A. Schildberg, *Front Immunol* **2020**, 11, 58.

[61] L. Xiao, Y. Ma, R. Crawford, J. Mendhi, Y. Zhang, H. Lu, Q. Zhao, J. Cao, C. Wu, X. Wang, Y. Xiao, *Materials Today* **2022**.

[62] Z. Chen, A. Bachhuka, S. Han, F. Wei, S. Lu, R. M. Visalakshan, K. Vasilev, Y. Xiao, *ACS Nano* **2017**, 11, 4494.

[63] M. Goseki, S. Oida, A. Nifuji, S. Sasaki, *J Dent Res* **1990**, 69, 909.

[64] I. R. Kim, S. E. Kim, H. S. Baek, B. J. Kim, C. H. Kim, I. K. Chung, B. S. Park, S. H. Shin, *BMC Complement Altern Med* **2016**, 16, 333.

[65] C. Liang, A. Y. Park, J. Guan, *Nature Protocols* **2007**, 2, 329.

[66] H. Xie, Z. Cui, L. Wang, Z. Xia, Y. Hu, L. Xian, C. Li, L. Xie, J. Crane, M. Wan, G. Zhen, Q. Bian, B. Yu, W. Chang, T. Qiu, M. Pickarski, L. T. Duong, J. J. Windle, X. Luo, E. Liao, X. Cao, *Nature Materials* **2014**, 20, 1270.

[67] C. D. Lucas, C. B. Medina, F. A. Bruton, D. A. Dorward, M. H. Raymond, T. Tufan, J. I. Etchegaray, B. Barron, M. Oremek, S. Arandjelovic, E. Farber, S. Onngut-Gumuscu, E. Ke, M. Whyte, A. G. Rossi, K. S. Ravichandran, *Sci Immunol* **2022**, 7, m4032.

[68] X. Zhang, W. Jiang, C. Xie, X. Wu, Q. Ren, F. Wang, X. Shen, Y. Hong, H. Wu, Y. Liao, Y. Zhang, R. Liang, W. Sun, Y. Gu, T. Zhang, Y. Chen, W. Wei, S. Zhang, W. Zou, H. Ouyang, *Nature Communation* **2022**, 13.

[69] F. Jiang, Y. Gao, C. Dong, S. Xiong, Biochem Biophys Res Commun 2018, 504, 734.

[70] X. Ma, Z. Jiang, N. Li, W. Jiang, P. Gao, M. Yang, X. Yu, G. Wang, Y. Zhang, *Aging* **2019**, 11, 10610.

[71] J. Fisher, G. Card, Y. Liang, B. Trent, H. Rosenzweig, L. Soong, *PLoS Pathog* **2021**, 17, e1009782.

[72] T. Matsubara, K. Suardita, M. Ishii, M. Sugiyama, A. Igarashi, R. Oda, M. Nishimura, M. Saito, K. Nakagawa, K. Yamanaka, K. Miyazaki, M. Shimizu, U. K. Bhawal, K. Tsuji, K. Nakamura, Y. Kato, *J Bone Miner Res* **2005**, 20, 399.

[73] M. Wang, Y. Yu, K. Dai, Z. Ma, Y. Liu, J. Wang, C. Liu, Biomater Sci 2016, 4, 1574.

[74] K. L. Spiller, R. R. Anfang, K. J. Spiller, J. Ng, K. R. Nakazawa, J. W. Daulton, G. Vunjak-Novakovic, *Biomaterials* **2014**, 35, 4477.

[75] Z. W. Zheng, Y. H. Chen, D. Y. Wu, J. B. Wang, M. M. Lv, X. S. Wang, J. Sun, Z. Y. Zhang, *Theranostics* **2018**, 8, 5482.

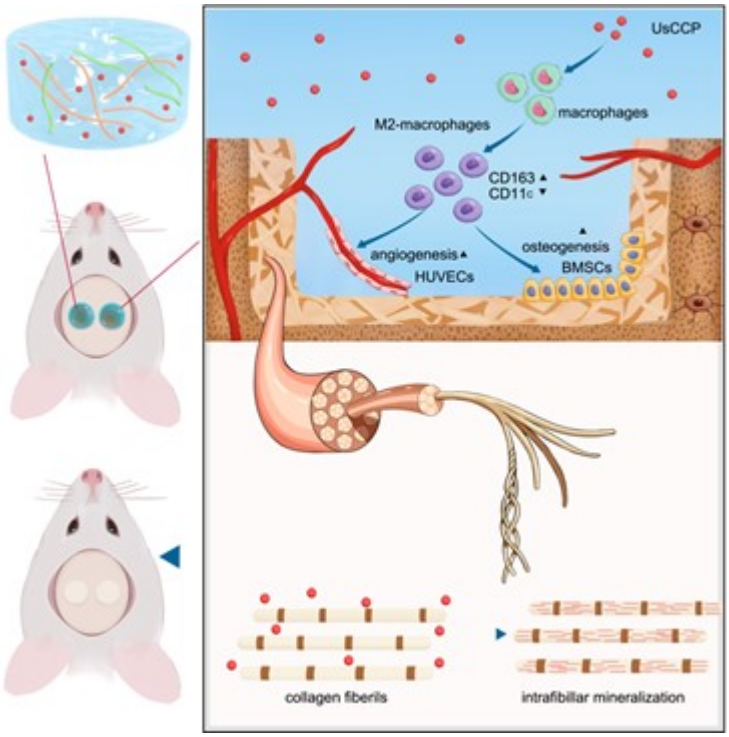

The scaffold was designed and developed based on the biomimetic mineralization theory, containing ultra-small particle size calcium phosphate nanocluster (UsCCP) with its 1-2 nm size. It could enhance bone strength characteristics by promoting intrafibrillar remineralization and promote the M2 type polarization of macrophages, thus to form an immune microenvironment conducive to osteogenesis and angiogenesis.